

Observations and modeling of ice cloud shortwave spectral albedo during the Tropical Composition, Cloud and Climate Coupling Experiment (TC⁴)

Bruce C. Kindel,¹ K. Sebastian Schmidt,² Peter Pilewskie,¹ Bryan A. Baum,³ Ping Yang,⁴ and Steven Platnick⁵

Received 31 August 2009; revised 22 January 2010; accepted 24 March 2010; published 15 September 2010.

[1] Ice cloud optical thickness and effective radius have been retrieved from hyperspectral irradiance and discrete spectral radiance measurements for four ice cloud cases during the Tropical Composition, Cloud and Climate Coupling Experiment (TC⁴) over a range of solar zenith angle (23°–53°) and high (46–90) and low (5–15) optical thicknesses. The retrieved optical thickness and effective radius using measurements at only two wavelengths from the Solar Spectral Flux Radiometer (SSFR) irradiance and the Moderate Resolution Imaging Spectroradiometer Airborne Simulator (MAS) were input to a radiative transfer model using two libraries of ice crystal single-scattering optical properties to reproduce spectral albedo over the spectral range from 400 to 2130 nm. The two commonly used ice single-scattering models were evaluated by examining the residuals between observed spectral and predicted spectral albedo. The SSFR and MAS retrieved optical thickness and effective radius were found to be in close agreement for the low to moderately optically thick clouds with a mean difference of 3.42 in optical thickness (SSFR lower relative to MAS) and 3.79 μm in effective radius (MAS smaller relative to SSFR). The higher optical thickness case exhibited a larger difference in optical thickness (40.5) but nearly identical results for effective radius. The single-scattering libraries were capable of reproducing the spectral albedo in most cases examined to better than 0.05 for all wavelengths. Systematic differences between the model and measurements increased with increasing optical thickness and approached 0.10 between 400 and 600 nm and selected wavelengths between 1200 and 1300 nm. Differences between radiance and irradiance based retrievals of optical thickness and effective radius error sources in the modeling of ice single-scattering properties are examined.

Citation: Kindel, B. C., K. S. Schmidt, P. Pilewskie, B. A. Baum, P. Yang, and S. Platnick (2010), Observations and modeling of ice cloud shortwave spectral albedo during the Tropical Composition, Cloud and Climate Coupling Experiment (TC⁴), *J. Geophys. Res.*, 115, D00J18, doi:10.1029/2009JD013127.

1. Introduction

[2] Ice clouds play an important role in the radiative budget of Earth's atmosphere [see, e.g., *Chen et al.*, 2000; *Ramanathan et al.*, 1989]. The scattering and absorption of solar radiation reduces the amount of energy reaching

the surface and thus has a cooling effect. Conversely, in the terrestrial thermal infrared wavelengths, ice clouds absorb radiation and emit at a lower temperature than Earth's lower atmosphere and surface. This reduces the amount of energy radiated to space, increases the downward infrared radiation, and warms the surface. Whether ice cloud top of the atmosphere (TOA) net radiative effect is cooling or heating is dependent on several factors including cloud height, cloud thickness, and cloud microphysics [*Stephens et al.*, 1990; *Ebert and Curry*, 1992; *Jensen and Toon*, 1994; *Baran*, 2009], for example. Ice cloud microphysical, optical and ice bulk properties that determine the radiative properties of clouds are perhaps the least well understood of these.

[3] Liquid water cloud radiative transfer calculations utilize Lorenz-Mie theory, an exact computational method for calculating the single-scattering properties (e.g., single-scattering albedo and phase function or its first moment, called the asymmetry parameter) of homogeneous spheres.

¹Laboratory for Atmospheric and Space Physics, Department of Atmospheric and Oceanic Sciences, University of Colorado at Boulder, Boulder, Colorado, USA.

²Department of Atmospheric and Oceanic Sciences, University of Colorado at Boulder, Boulder, Colorado, USA.

³Space Science and Engineering Center, University of Wisconsin-Madison, Madison, Wisconsin, USA.

⁴Department of Atmospheric Sciences, Texas A&M University, College Station, Texas, USA.

⁵NASA Goddard Space Flight Center, Greenbelt, Maryland, USA.

In contrast to liquid water droplets, nonspherical ice cloud particles encompass a wide variety of shapes and sizes and thus computing their radiative properties must rely on more involved numerical techniques. To this end, extensive modeling and some measurements of ice crystal single-scattering properties have been undertaken [Takano and Liou, 1989; Macke et al., 1996; Baum et al., 2005; Yang and Liou, 1998; Yang et al., 1997, 2003; Mishchenko et al., 1996; Baran et al., 1999; Baran, 2004; Baran and Labonnote, 2007; Baran and Havemann, 2004; Ulanowski et al., 2006] and continues to be an area of active research.

[4] These models are used for satellite remote sensing retrievals of cloud optical properties (e.g., MODIS, AVHRR, etc.) [King et al., 1992; Platnick et al., 2003]. Ultimately, these types of satellite retrievals are used: as inputs to climate models to properly parameterize ice cloud radiative effects [Stephens et al., 1990; Fu, 2007; Edwards et al., 2007], to potentially improve ice water parameterization in global circulation models [Waliser et al., 2009], and to aid in the study of ice cloud processes [Jiang et al., 2009].

[5] One of the main purposes of this study was to examine how well the models of single-scattering optical properties of ice particles can reproduce the spectral albedo of ice clouds encountered during TC⁴. Satellite retrievals of cloud optical thickness and effective radius are typically retrieved at just two spectral bands, one in the visible to very near-infrared where ice and liquid water are nonabsorbing and the other in the shortwave infrared where ice and liquid water weakly absorb. The former is most sensitive to cloud optical thickness, the latter to cloud particle size. For a complete description of this type of retrieval, see Twomey and Cocks [1982] or Nakajima and King [1990].

[6] Current models of ice single-scattering properties contain far more than two wavelengths. The models used in this study contains 140–150 wavelengths [Yang and Liou, 1998; Baum et al., 2005] spread across the solar spectrum. In principle, if the model of the single-scattering is spectrally accurate, then the retrieved optical thickness and effective radius from as few as two wavelengths should accurately predict the spectral albedo for the entire spectrum for plane-parallel, homogenous, single layer clouds. By retrieving the optical properties of ice clouds, using the classical two wavelength technique, one should be able to test, at the very least, how consistent the wavelength to wavelength albedo is modeled by comparing with spectral measurements of albedo from the Solar Spectral Flux Radiometer (SSFR).

[7] A previous study was conducted comparing the retrieval of optical properties from solar wavelengths with thermal wavelengths [Baran and Francis, 2004]. It was shown that when the incorrect ice single-scattering model was used the results were physically inconsistent; for the same cloud scene the incorrect ice model did not simultaneously retrieve the same values of optical thickness and effective radius across both the solar and thermal spectrum. This study argued for high-resolution measurements across the spectrum (solar and thermal wavelengths) to discriminate between ice models. Here we have examined the spectral consistency at high spectral resolution and sampling over the majority of the solar spectrum, at optical thicknesses ranging from 3 to 46 and solar zenith angles ranging from 23° to 53°. Unlike the Baran and Francis [2004] study, we have not

examined the thermal portion of the spectrum but instead have focused solely on the solar portion of the spectrum, extending the wavelength range further into the near-infrared, covering several zenith angles, comparing hundreds of spectra, and using hyperspectral irradiance in addition to multispectral radiance measurements for comparison. Because many remote sensing retrievals of cloud optical thickness and effective radius rely on these single particle scattering models testing their spectral fidelity is an important validation. The accuracy of the models cannot be judged solely from remote sensing measurements as it implies some level of circularity because the scattering models themselves are necessary for the retrieval of optical thickness and effective radius. It would be preferable, for instance, to have an independent measurement of particle size that does not rely on ice-scattering models. Particle size measurements, in situ, were made during TC⁴, but are prone to crystal shattering [McFarquhar et al., 2007; Jensen et al., 2009]. Even in the absence of in situ measurement errors like inlet shattering, issues of cloud volume sampling (small and usually deep within a cloud for in situ measurements; large and near cloud top for radiation measurements) also confound efforts at comparing the two. For these reasons, no in situ data were used.

[8] A second focus of this study was a comparison of irradiance and radiance based retrievals of cloud optical properties. Satellite remote sensing retrievals are, by necessity, radiance based and implement observations from discrete wavelength bands distributed across the solar and terrestrial spectrum. A selection of channels from radiance-based remote sensing instruments is, by itself, insufficient to completely determine the effects of clouds on Earth's radiation budget. In practice, irradiance cannot be measured directly from space-borne platforms in low Earth orbit. It is, however, measured from aircraft. To bridge the fundamental geometrical and spectral differences between satellite measurements of discrete-band radiance and the more energetically relevant quantity, continuous spectral irradiance, field campaigns deploying instruments that measure discrete-band radiance and hyperspectral irradiance have been conducted: the Ice Regional Study of Tropical Anvils and Cirrus Layers-Florida Area Cirrus Experiment (CRYSTAL-FACE) [Jensen et al., 2004]; and the focus of the present study, the Tropical Composition, Cloud and Climate Coupling experiment (TC⁴) [Toon et al., 2010]. In TC⁴ the high-altitude NASA ER-2 flew with the SSFR, which measured spectrally continuous solar irradiance (400–2200 nm), and the MODIS Airborne Simulator (MAS), a discrete-band imaging spectrometer that measured solar reflected and thermal emitted radiance (550–14200 nm).

[9] This paper is organized as follows: (1) the measurements of spectral irradiance from the SSFR and radiance imagery from MAS; (2) models of single-scattering optical properties and their incorporation into a radiative transfer model along with the method employed for retrieving the optical thickness, effective radius, and albedo; (3) cloud optical thickness and effective radius retrieved from MAS radiance and SSFR irradiance using two currently available ice single-scattering libraries; (4) the spectral albedo calculated from a two-wavelength SSFR retrieval compared with the measured spectral albedo and also the spectral albedo calculated from a two-wavelength MAS radiance retrieval

compared with the measured spectral albedo; (5) individual spectra for high and low optical thickness and effective radius from each case; and (6) a summary of the work.

2. Measurements of Radiance and Irradiance During TC⁴

[10] The NASA ER-2 was instrumented with the SSFR and either the MODIS Airborne Simulator (MAS) [King *et al.*, 2004] or the MODIS/ASTER (MASTER) airborne simulator [Hook *et al.*, 2001] for thirteen flights together over the course of the experiment. These flights covered a wide variety of cloud types, including extensive fields of low marine stratus, tropical convective systems, and high tropical ice clouds, which is the focus of this paper. Because only data from the MAS instrument were ultimately used in this work, only the MAS instrument will be described in detail.

2.1. Solar Spectral Flux Radiometer

[11] The SSFR consists of two spectroradiometers connected via a fiber optic to a miniature integrating sphere mounted on the top (zenith viewing) and bottom (nadir viewing) of the NASA ER-2. The integrating spheres provide the cosine response over the wide wavelength range of the SSFR that is required to make a measurement of spectral irradiance. The wavelength range of the instrument, 350 to 2150 nm, encompasses 90% of incident solar radiation. The spectral resolution as measured by the full-width-half-maximum (FWHM) of a line source is 8 nm from 400 to 1000 nm with 3 nm sampling and 12 FWHM from 1000 to 2200 nm with 4.5 nm sampling. The SSFR records a nadir and zenith spectrum every second.

[12] The spectrometers are calibrated in the laboratory with a NIST-traceable blackbody (tungsten-halogen 1000 W bulb). The radiometric stability of the SSFR is carefully tracked during the course of a field experiment with a portable field calibration unit with a highly stable power source and 200 W lamps. The calibration has generally held to the 1 to 2% level over the course of a several week field mission as it did during TC⁴. The radiometric calibration was adjusted for minor fluctuations measured by the field calibration from flight to flight. In addition, the data were filtered using the aircraft navigation and ephemeris data to eliminate time periods when the aircraft attitude was not level (e.g., turns, takeoff and landing, turbulence). The estimated uncertainties in the absolute calibration of the instrument are 5%. We note that when retrieving cloud optical properties with albedos, as was done here, error in the absolute calibration cancel. Errors from unknown offsets in aircraft navigation data or reflections from clouds may remain however. For a more complete description of the SSFR instrument see [Pilewskie *et al.*, 2003].

2.2. MODIS Airborne Simulator

[13] The MAS instrument is an imaging spectrometer with 50 discrete bands distributed throughout the solar reflected and thermal emitted parts of the spectrum. Twenty-two of the bands in the solar region overlap with the SSFR from 461 to 2213 nm. The spectral bandpass of MAS in the visible and near-infrared channels are in the range of 40–50 nm, it has a 2.5 mrad instantaneous field of view (IFOV), and 16 bit analog to digital conversion. MAS is typically preflight and

postflight calibrated in the laboratory with an integrating sphere and uses an integrating hemisphere in the field for stability monitoring. For details on MAS calibration issues and investigations during TC⁴, see King *et al.* [2010]. Because it is an imager, it provides excellent spatial context (~25 m nadir pixel resolution with ~17 km swath width for typical TC⁴ ice cloud heights) with which to help interpret the measurements of irradiance from SSFR.

[14] All thirteen flights and all flight legs therein were examined with the MAS or MASTER cloud products which includes cloud optical thickness, cloud phase, cloud top height, and temperature information. The flight legs used in this study were selected on the basis of several criteria: the abundance of ice clouds; legs that were only over open ocean to simplify the input of surface spectral albedo into the radiative transfer calculations; the apparent absence of low-level clouds which might make the retrieval of ice cloud properties more complicated and prone to error (an example of this which occurred frequently in the data are low-level cumulus clouds, presumably liquid water, beneath an optically thin layer of ice cloud); and finally, stable, level flight which is required for the measurement of irradiance. Four flight tracks from 17 July 2007 (the ER-2 was equipped with MAS instrument that day) met these criteria and were used for analysis in this work. The cosine of the mean solar zenith angle (denoted by μ) for the four flight legs were 0.60, 0.82, 0.88, and 0.92. For the remainder of this paper the four cases will be distinguished by their cosine of solar zenith angle (i.e., the $\mu = 0.82$ case, the $\mu = 0.88$ case, etc.). Of these cases, three ($\mu = 0.60, 0.82, 0.88$) had low to moderate optical thickness (3–15), and one case ($\mu = 0.92$) had high optical thickness (40–50).

2.3. Radiative Transfer Calculations of Irradiance

[15] Analysis of solar spectral irradiance from SSFR has led to the development of a radiative transfer code optimized for the spectral characteristics of the SSFR and for flexibility in specifying cloud and aerosol radiative properties [Bergstrom *et al.*, 2003; Coddington *et al.*, 2008]. The molecular absorption by species such as water vapor, oxygen, ozone, and carbon dioxide, are calculated using the correlated-k method [Lacis and Oinas, 1991]. The band model was developed specifically for the SSFR by defining the spectral width of the bands by the slit function of the SSFR spectrometers, the full-widths of which were noted previously. The k-distribution is based on the HITRAN 2004 high-resolution spectroscopic database [Rothman *et al.*, 2005]. The model uses the discrete ordinate radiative transfer method (DISORT) [Stamnes *et al.*, 1988] to solve for the spectral irradiance and nadir and zenith radiance at each level. Molecular-scattering optical thickness is calculated using the analytical method of Bodhaine *et al.* [1999]. The model contains 36 levels. In this study albedo was calculated at 20 km, the nominal flight level of the ER-2. The albedo is defined as the ratio of upwelling to downwelling irradiance at the flight level. A standard tropical atmospheric profile of water vapor and well mixed radiatively active gases was used. No attempt was made to fit the water vapor amount to match the measurements; this would be computationally prohibitive and unnecessary, because the absorption bands of water vapor, oxygen, etc., are avoided for inferring cloud optical properties. The wavelengths used for the cloud retrieval of optical

thickness and effective radius are 870 and 1600 nm. These wavelength channels are free of strong gaseous absorption.

[16] No aerosol was included in the model because these are tropical, high-level clouds, and are unlikely to contain much aerosol. The top of the atmosphere (TOA) solar spectrum is given by the Kurucz spectrum [Kurucz, 1992]. The input surface albedo (always ocean) was specified by constant value of 0.03 [Jin *et al.*, 2004].

[17] The input to the radiative transfer model first requires that the phase function of the ice particles be represented in terms of a Legendre polynomial series where the number of terms is set to the number of streams used in the DISORT calculation. All of the DISORT calculations for this study were done with 16 streams with Delta-M scaling [Wiscombe, 1977] to account for the strong forward scattering peak in the phase function typical of large size parameters. For the accurate calculation of irradiance at least six streams are required; streams are the number of quadrature points in the angular integration of scattering. We used the technique of Hu *et al.* [2000] to fit the phase function with the Legendre coefficients for input into the radiative transfer model.

[18] Clouds heights for these cases were examined using the MAS cloud height product and were found to vary from between 8 to 12 km. A cloud height sensitivity test was performed by setting a cloud deck to 12 and to 8 km, for the retrieval of cloud optical properties. Little to no change in the retrieved values was found, so that the calculation was set to 10 km for all of the cases. This is the result of using 870 nm as one of the retrieval wavelengths. The molecular scattering is reduced at this wavelength and the effect on the retrieval of cloud height was small. The use of a shorter wavelength (e.g., 500 nm) would likely show a greater sensitivity to cloud height.

[19] The effects of cloud vertical [Platnick, 2000] and horizontal [Platnick, 2001; H. Eichler, Cirrus spatial heterogeneity and ice crystal shape: Effects on remote sensing of cirrus optical thickness and effective crystal radius, submitted to *Journal of Geophysical Research*, 2010] inhomogeneity on the retrieval of cloud optical properties have been investigated previously. For clouds with varying vertical and/or horizontal microphysical structure, the use of different wavelengths in the inversion procedure may result in different values of retrieved effective radius. However, these differences are typically small compared to retrieval errors [Platnick, 2000; Ehrlich *et al.*, 2009]. In this paper, all calculations were done assuming plane-parallel, homogenous (vertically and horizontally) clouds. The impact of vertical or horizontal cloud inhomogeneities on retrievals of optical thickness and effective radius was not investigated in this work.

2.4. Ice Particle Single-Scattering Models

[20] The ice crystal single-scattering models used here are the same ones used for the MODIS Collection 4 [Baum *et al.*, 2000; Platnick *et al.*, 2003; Yang and Liou, 1996, hereinafter referred to as C4] and Collection 5 cloud products [Baum *et al.*, 2005, hereinafter referred to as C5]. The C4 models consist of plates, hollow and solid columns, 2-D bullet rosettes, and aggregates consisting of solid columns. The C4 ice crystal-scattering model provide scattering properties for 5 size bins and were integrated over 12 particle size distributions. The range of effective radii in C4 is 6.7 to 59 μm

with a total of twelve effective radii. The small particles in C4 are assumed to be compact hexagonal ice particles. The results from C4 (see Figures 6 and 7, blue plots), used in the MODIS collection 4 [Platnick *et al.*, 2003] are shown primarily because it has continuous spectral coverage from 400 to 1695 nm and fills in some of the spectral regions not covered in C5. The resultant albedo spectra produced using C4 and C5 ice particle-scattering models produced very similar spectra as will be shown in Figures 6 and 7.

[21] The more recently developed C5 models consist of mixtures of different ice particle shapes (e.g., droxtals, solid and hollow columns, plates, 3-D bullet rosettes, and aggregates of columns). The scattering properties for each of these particles are available for 45 individual size bins. For both sets of bulk models, all particles are smooth except for the aggregate, which is roughened. The roughening parameter is 0.3 (B. A. Baum, personal communication, 2009). For C5 the ice particles range in size from 5 to 90 microns in a step size of ten microns for a total of eighteen different effective radii. The wavelength coverage is from 400 to 2200 nm, matching the SSFR coverage. The database contains some spectral gaps, in the regions 1000–1200 nm, 1700–1800 nm, and 1950–2050 nm. Outside of the gaps the spectral sampling is 10 nm. Each size regime in the model consists of a different mixture; the smallest consists of only droxtals for C5, the largest is predominantly bullet rosettes. Intermediate sizes are varying mixtures of shapes. The relative contribution of each particle shape to the size distribution is different between C5 and C4; Yang *et al.* [2007] gives a detailed summary of each.

[22] The single-scattering properties include a scattering phase function defined at 498 angles between 0° and 180°, asymmetry parameter, extinction efficiency, extinction and scattering cross sections, single-scattering albedo (ω_0), and a delta transmission factor (δ). The delta transmission factor is wavelength dependent and is used to scale the input optical thickness (τ) and single-scattering albedo in the radiative transfer model according to equations 1 and 2.

$$\omega'_0 = \frac{(1 - \delta)\omega_0}{1 - \delta\omega_0} \quad (1)$$

The primed quantities are the δ -scaled values of optical thickness and single-scattering albedo. The δ transmission factor is used to account for transmission through plane parallel ice particle planes in the forward direction; that is, at a scattering angle of zero degrees [Joseph *et al.*, 1976; Takano and Liou, 1989]. The effective radius is defined by equation (2), where $\langle V \rangle$ is the mean particle geometric volume and $\langle A \rangle$ is the orientation-averaged projected area for the ice crystal size distribution [McFarquhar and Heymsfield, 1998; Mitchell, 2002].

$$r_{\text{eff}} = \frac{3}{4} \frac{\langle V \rangle}{\langle A \rangle} \quad (2)$$

[23] Figure 1 shows an example of the library phase function at 870 nm for the largest (solid line) and smallest (dash-dot line) effective radii in C5. Figure 1 also shows the single-scattering albedo wavelength spectra of a smallest and largest size effective radii (C5). The phase function for the largest size exhibits ice halo features at 22 and 46 degrees; the phase function for the smallest particle size is notably

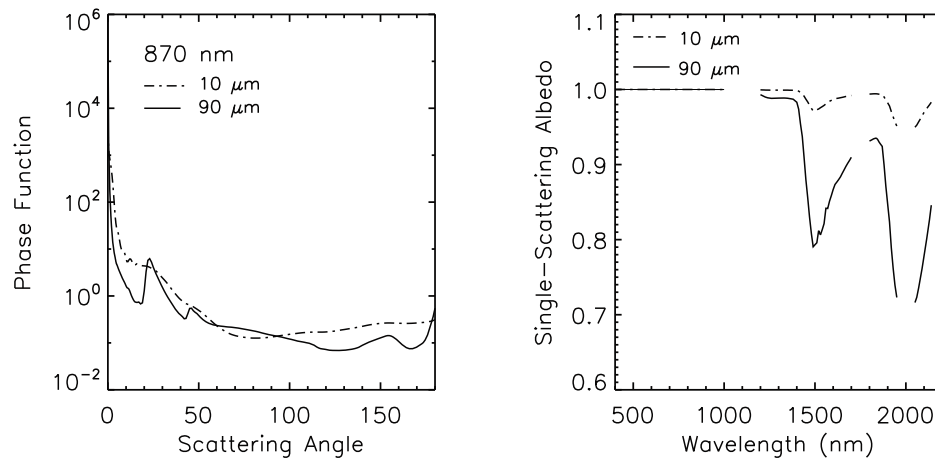


Figure 1. (left) Phase functions at 870 nm from the C5 library for the largest (90 μm , solid line) and smallest (10 μm , dash-dot line) effective radii. (right) Single-scattering albedo spectra for the largest (solid line) and smallest (dash-dot line) effective radii from the C5 library.

smoother. The differences in phase functions are a result of both particle size, shape, and the differences in particle mixtures which are different for each effective radius. In the shortwave infrared the single-scattering albedo for the largest size is reduced below that of the smallest size, as expected from simple geometric optics [Bohren and Huffman, 1983]. This forms the basis for the retrieval of effective radius in this spectral regime. Ice is essentially nonabsorbing in the visible. To generate an albedo library for each case, a series of cloud optical thicknesses, thirty in total, were calculated for each of the four solar zenith angles. Optical thickness step sizes range from 0.5 at the smallest optical thickness, to 2 to 5, at intermediate optical thickness, and 10 at the highest optical thickness (50–100). All optical thickness values given in this paper are for 870 nm. The resolution in the calculation of the various effective radii was given by the single-scattering ice library employed; eighteen in the case of the C5, twelve for the C4 library. The C4 library is not evenly spaced in effective radius; it contains finer sampling in the range of 25 to 40 μm . At this resolution, the spectra are sufficiently smooth so they can be interpolated with a high degree of accuracy to generate a finer optical thickness and effective radius grid. The optical thickness grid was linearly interpolated to increments of 0.1 from endpoints of the calculations, 0–100. The effective radii were linearly interpolated to a step size of 0.2 from the range of 5 to 90 μm in the C5 library and 6.7 μm to 59 μm in the C4 library. Figure 2 shows a range of optical thickness and effective radius of the calculated albedo spectra. The optical thicknesses are color coded and the effective radii are line style coded. Note that the spectra group by color in wavelengths between 400 and 1000 nm and contain information about optical thickness; the spectra cluster by line style for the wavelengths 1500 to 2150 nm, and contain information about effective radius.

3. Retrieval of Optical Thickness and Effective Radius From SSFR and MAS

[24] For the retrieval of optical thickness and effective radius at least two wavelengths are chosen to determine a best fit to the calculated spectra. Previous work with

retrievals from the SSFR has included up to five wavelengths [Coddington et al., 2008]. Others have investigated the utility of including more than two wavelengths [Cooper et al., 2006; Baran et al., 2003]. The authors of these studies have advocated the use of more than two wavelengths in the retrieval of cloud optical properties for a more robust result. Because wavelength selection was not the focus of this study and comparison of SSFR and MAS retrievals was desired, we have chosen to follow the technique used in satellite retrievals and use the MAS wavelengths: 870 nm (water nonabsorbing) and 1600 or 2130 nm (water absorbing). Measurement to measurement variation was smaller at 1600 nm for SSFR, so it was chosen for the water-absorbing wavelength applied in this analysis. A two step process was implemented as follows. The first step is an initial estimate from the uninterpolated data to determine the range that the measurement falls in; that

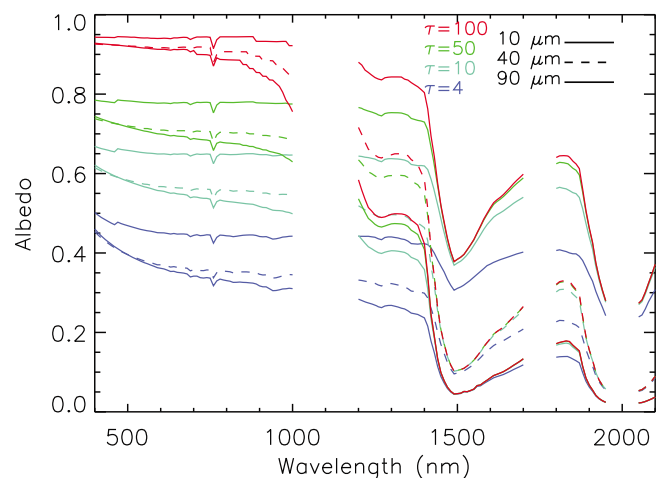


Figure 2. The results of the C5 library in the radiative transfer calculations of albedo spectra for three different effective radii and four different optical thicknesses. The spectra cluster by color (optical thickness) in the 400–1000 nm wavelength range, and by line style (effective radius) in the 1500–2150 nm wavelength range.

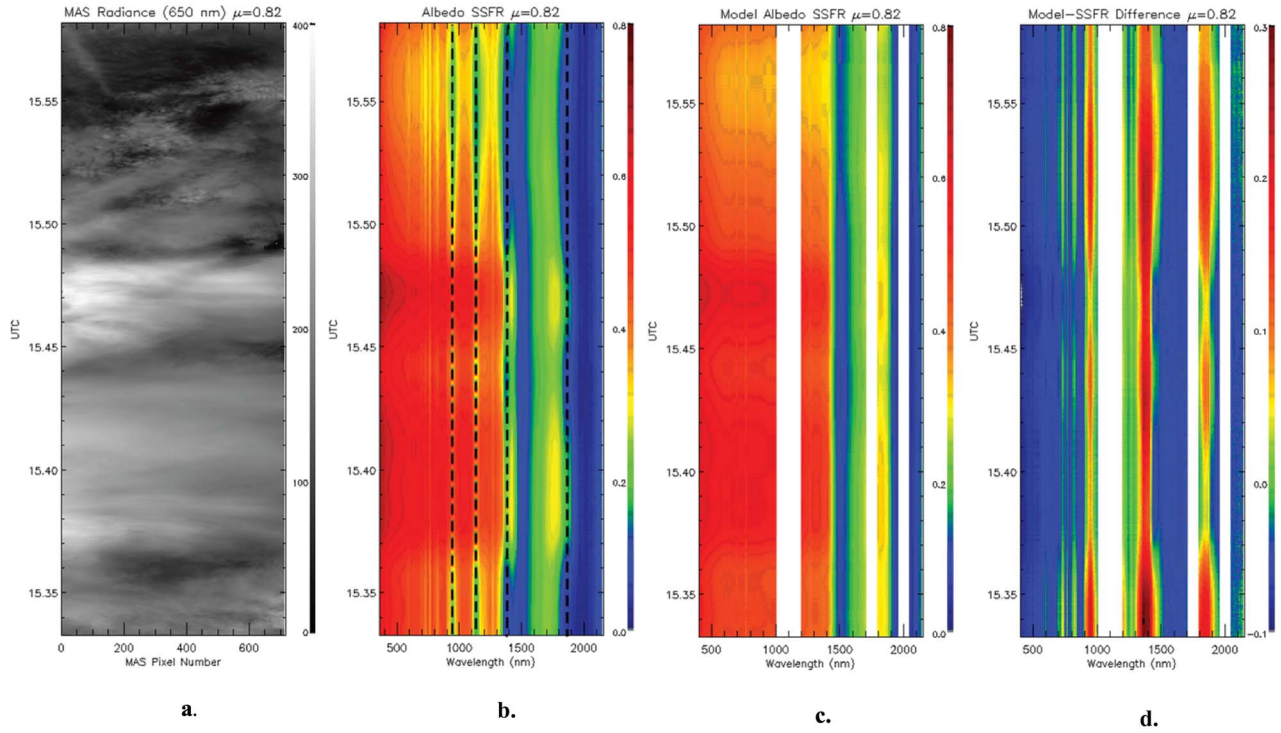


Figure 3. Two-dimensional representations of the $\mu = 0.82$ case. (a) MAS radiance at 650 nm. (b) SSFR-measured albedo with wavelength on the x axis. (c) Calculated albedo using optical thickness and effective radius retrieved from SSFR. (d) Difference image between Figures 3b and 3c.

range is used to constrain the retrieval in the interpolated data. This greatly increases the speed at which a minimum in the least squares fit is found, over the search of the entire high-resolution library for each measurement. The “best fit” is determined by minimizing the residual in a least squares sense (equation 3), of the measurement to calculated albedo value at the given wavelengths.

$$\text{residual} = (vis_{\text{measured}} - vis_{\text{model}})^2 + (nir_{\text{measured}} - nir_{\text{model}})^2 \quad (3)$$

The calculation of optical thickness and effective radius for MAS is given by the MAS algorithm [King *et al.*, 1997; King *et al.*, 2004] and is identical to that used for MODIS-derived cloud optical properties. The MAS-derived optical thickness and effective radius are the results of the NASA retrieval scheme and use the MODIS Collection 5 (C5) ice properties. No separate attempt was made to retrieve cloud optical properties with the MAS radiance data.

4. Analysis of Spectral Albedo Properties

[25] To test the ability of single-scattering models to accurately reproduce the observed spectral albedo, we retrieved the optical thickness and effective radius using SSFR albedo at two wavelengths from each spectrum coincident with the MAS flight legs. The retrieved optical thickness and effective radius were then used to calculate the entire spectrum with the radiative transfer model. Figure 3a shows the MAS 650 nm radiance for the $\mu = 0.82$ case; time (UTC) is

along the y axis, the cross-track swath of MAS along the x axis. Figure 3b shows the spectral albedo measured by the SSFR. Wavelengths varies along the x axis, time is on the y axis. Note the strong water vapor absorption in the measurements at 1400 nm and 1900 nm, and weaker bands at 940 and 1140 nm, all represented by vertical bands in the image. The approximate band centers (940, 1140, 1400 and 1900 nm) of water vapor are over plotted with black dashed lines. Figure 4 shows a typical SSFR albedo spectrum with the water vapor band centers and band widths shown to aid in interpreting the spectra. Figure 3c shows the spectral albedo reconstructed from the two-wavelength SSFR retrieval of the cloud optical thickness and effective radius. The white bands are the aforementioned spectral gaps in the ice-crystal model data (C5). There is little evidence of water vapor absorption in this image. A comparison of Figures 3b and 3c provides evidence that an insufficient amount of water vapor was used in the model but it is of no consequence in the present analysis because those bands were avoided in the retrievals. Image 3d shows the difference between the reconstructed albedo and the SSFR measured albedo. In this flight segment the optical thickness varied from 5 to 15 (see Figure 9 for the time series) and the effective radius varied from 25 to 35 μm . The difference image varies little over this change in optical thickness and effective radius, indicating that the single-scattering optical properties given in C5 capture the range of possible single-scattering properties needed to accurately reproduce the spectral albedos that were encountered during the flights examined here. Indeed, the difference plots for the $\mu = 0.88$ and $\mu = 0.60$ cases

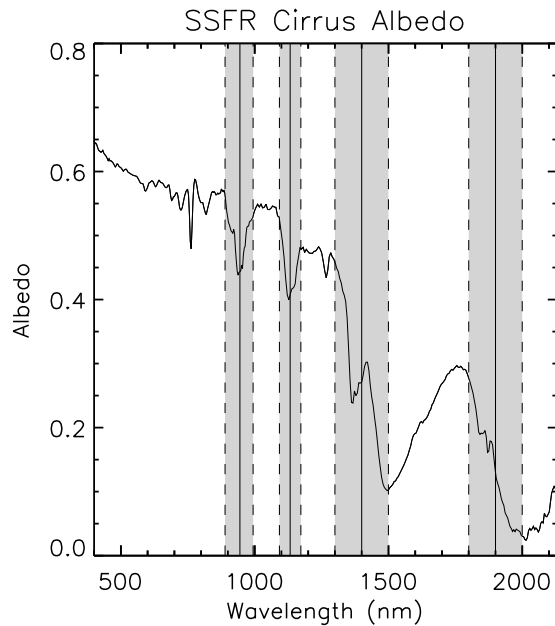


Figure 4. A typical SSFR cloud albedo spectrum is plotted with the major water vapor band centers (940, 1140, 1400, and 1900 nm) overplotted with vertical lines. The approximate band widths are the shaded regions bounded by the dashed lines.

(not shown) are virtually identical to the $\mu = 0.82$ case shown here. The $\mu = 0.92$ case is somewhat different as will be discussed later in the paper when examining individual spectra.

[26] In general, the differences outside of strong molecular gaseous absorption bands fall within 0.05 of the measured albedo. Larger differences occur in water vapor bands. These bands are highly variable and no effort was made to vary the standard tropical water vapor profile. All four cases examined here fall within moderate to high optical thicknesses. For the cloud optical thicknesses examined here, all substantially greater than unity, the spectral albedo is only weakly sensitive to particle shape [Wendisch *et al.*, 2005]. The effects of absorption are amplified through multiple scattering while angularly-dependent scattering features are diminished. In Figure 5 the differences for all times are plotted at each wavelength showing the entire range of differences for all wavelengths (the small black dots that in aggregate form a line). Superimposed (red diamonds) is the calculated mean albedo difference at each wavelength. The albedo differences are typically less than 0.05, with some exception. Many of largest deviations occur on the edges of strong molecular absorbers such as the 1400 and 1900 nm water vapor wings or the strong oxygen band at 763 nm and are the result of gaseous absorption.

[27] The $\mu = 0.88$ case is the most spatially uniform, albeit short in duration, of the flight legs examined here; it has the smallest retrieved range and standard deviation in optical thickness. In terms of determining systematic differences between model and measurement, this is perhaps the best of the flight legs because spatial homogeneity is greatest. Wavelength to wavelength consistency (spectral shape) is

similar for all the cases, although the variation within a particular wavelength may be greater ($\mu = 0.92$) or lesser ($\mu = 0.82$). The differences at the shortest wavelengths could be explained by differences in molecular scattering and/or the presence of aerosols. However, further examination of the lidar data showed no evidence of aerosols above the clouds for these cases and the molecular-scattering component appears to be well modeled in the three moderate optical thickness cases. Because these errors are typically less than 0.03, and close to measurement error, no further refinement of the modeling was undertaken.

[28] The exception to this is the $\mu = 0.92$ case that had optical thicknesses substantially higher (33–46) than the other cases (3–15). At the shortest wavelengths the differences are 0.07–0.08. The spectral shape of the differences is similar to the others cases, but the magnitude is greater. This is true only of the shorter wavelengths; for the wavelengths longer than 1500 nm the agreement is within 0.02–0.03. The reason for this difference is unresolved. The largest systematic difference between measurement and model in all cases, outside of strong gas absorption, occurs in the 1200 to 1300 nm range. Although this region does contain a relatively narrow collision band of oxygen at 1270 nm the mismatch is much broader. This mismatch increases with increasing optical thickness, and is most evident for the $\mu = 0.92$ case that has substantially higher optical thickness than the other cases. This may indicate that the single-scattering albedo is too high in this spectral region as multiple scattering (high optical thickness) amplifies absorption. The ice single-scattering properties in C4 and C5 used the Warren [1984] compilation for the ice optical constants. A new compilation by Warren and Brandt [2008] contains substantial changes in the near-infrared complex part of the index of refraction. In particular, the spectral range in the 1500 to 2000 nm spectral range has changed. The imaginary part of the complex index of refraction has increased at 1600 nm (one of the retrieval wavelengths) and decreased from 1700 to 1900 nm. The reanalysis of the measurements used in the work of Warren [1984], better accounting for surface reflections, resulted in the changes made in the work of Warren and Brandt [2008]. These changes have been implemented in the most recent single-scattering ice calculations by the developers of C4 and C5, but were not available for this analysis. Simple calculations indicate that these changes alone are probably not sufficient to account for the differences in the measurement and model, thus the explanation for this discrepancy remains unresolved. In addition, the spectral region from 1000 to 1300 nm has not changed in the new compilation.

[29] A more detailed representation of the differences between the highest and lowest retrieved values of optical thickness and effective radius (four in total) for each of the four segments and its corresponding spectral albedo from SSFR is plotted in Figures 6 and 7. SSFR albedo spectra are plotted in black and are continuous; the red spectra were the reconstructed using C5, and the blue spectra C4. The regions of best agreement are from 1500 to 2100 nm, excluding the strong water vapor band at 1900 nm. For the case $\mu = 0.92$, the high optical thickness and height of the cloud reduce the water vapor absorption to the point where it ceases to interfere with the measurement of cloud albedo. This is because the

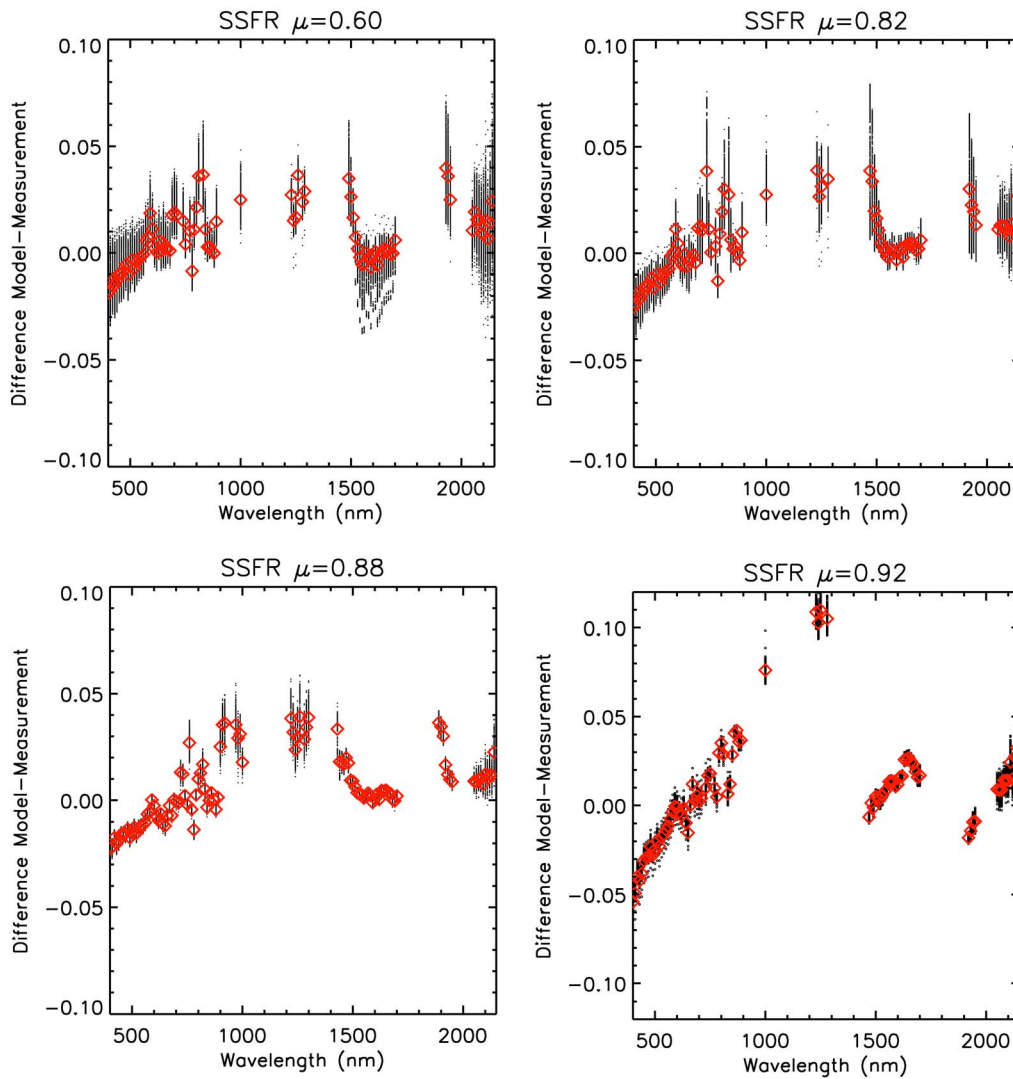


Figure 5. For each of the four cases the differences between modeled (C5) and measured albedo using optical thickness and effective radius derived from SSFR are shown. The black dots which aggregate to form lines are the differences for every line in the MAS flight track, and the red diamonds are the mean differences.

column water vapor above these high-altitude clouds is low and the contribution of water vapor absorption from below the cloud layer (owing to its high optical thickness) is small. In the lower optical thickness cases, we are seeing “through” the cloud layer and the contribution of water vapor absorption from below the cloud layer is much greater. The agreement is quite similar (0.02) to the surrounding spectrum where water vapor does not interfere with the ice cloud albedo. Note that in all the cases, as the optical thickness becomes larger, the mismatch between the modeled and measured spectra becomes larger in the 1200–1300 nm spectral region.

[30] The effective radii for the C5 based retrieval are smaller in general than those from C4. The optical thicknesses are generally greater for C5 than C4. This is in agreement with a comparison done for the MODIS 4 and MODIS 5 collections (based in part on C4 for MODIS 4 and C5 for MODIS 5) by *Yang et al.* [2007] that showed average optical thickness is greater by 1.2 from C5 (MODIS 5 collection) and an average

greater effective radius from C4 (MODIS 4 collection) of $1.8 \mu\text{m}$.

5. Comparison of Irradiance and Radiance-Derived Optical Properties

[31] The comparison of irradiance measurements (SSFR) and radiance (MAS) is challenging for several reasons. Perhaps the greatest of these is the difference in spatial sampling of the cloud field. MAS measures radiance over a finite swath width, 37 km at the ground. The SSFR measures the cosine weighted radiance integrated over the upward and downward hemispheres centered at the aircraft. To compare measurements from the two instruments the MAS radiance was spatially averaged following the analysis of *Schmidt et al.* [2007]. The technique averages MAS radiance over the half power point of the SSFR signal. The diameter of the SSFR half power point is approximately the MAS swath width, 17 km for a cloud deck at 10 km and an ER-2 altitude of

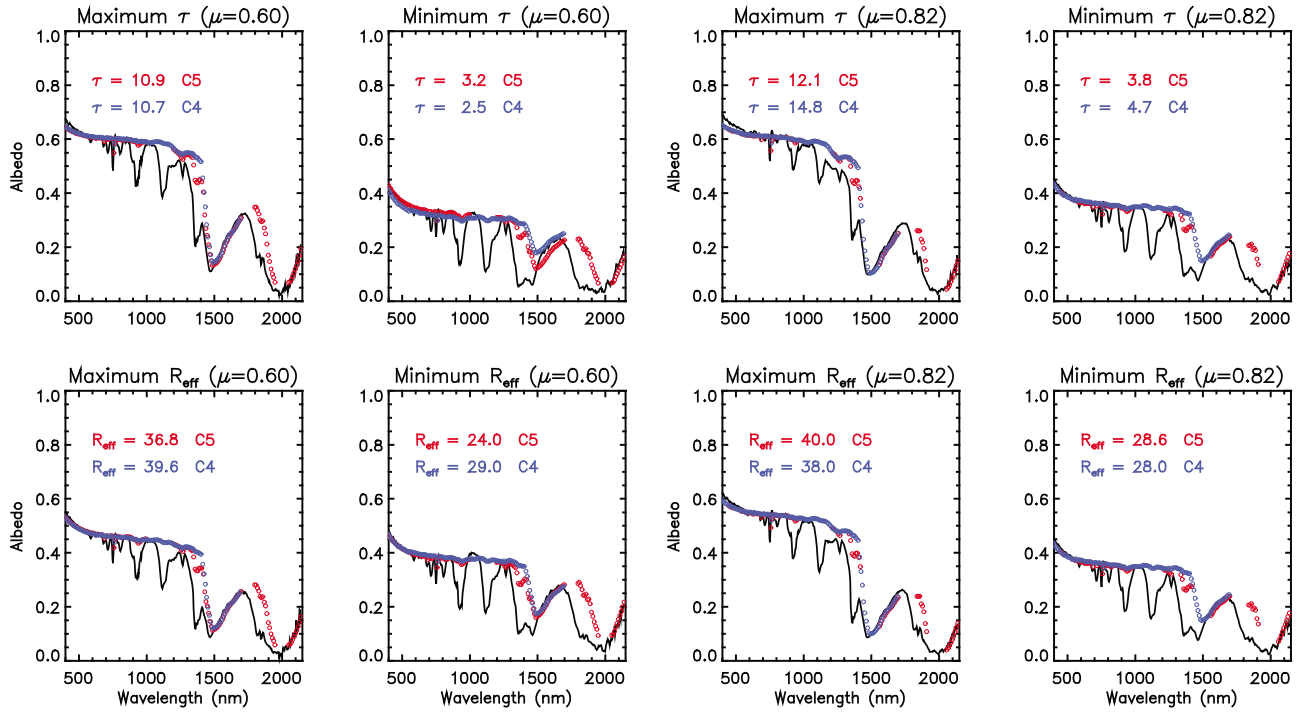


Figure 6. For cases $\mu = 0.60$ and $\mu = 0.82$ the highest and lowest optical thickness and effective radius albedo spectra are plotted with the full wavelength spectra as predicted from the single-scattering properties from C5 (red) and C4 (blue). Note the excellent agreement in all cases in the longer wavelength. As the optical thickness increases, the agreement becomes worse in the shorter wavelengths and in the 1200–1300 nm range.

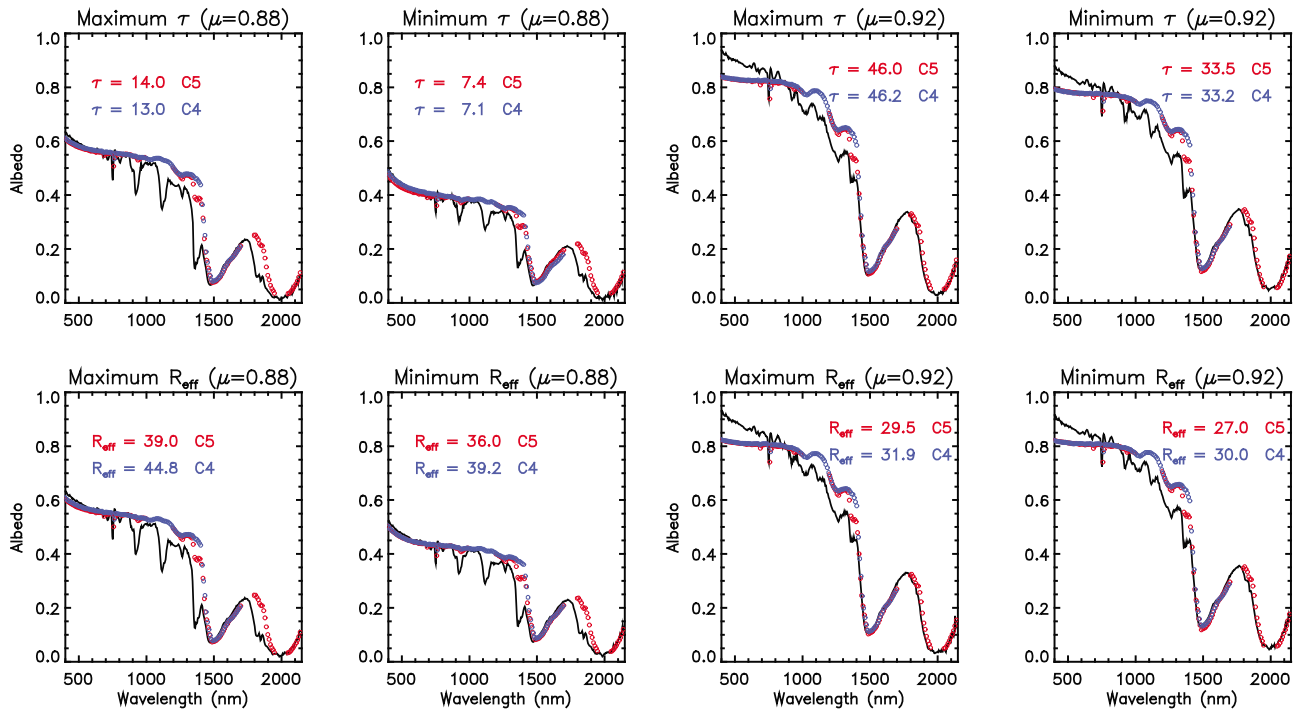


Figure 7. Same as Figure 6 but for the cases $\mu = 0.88$ and $\mu = 0.92$.

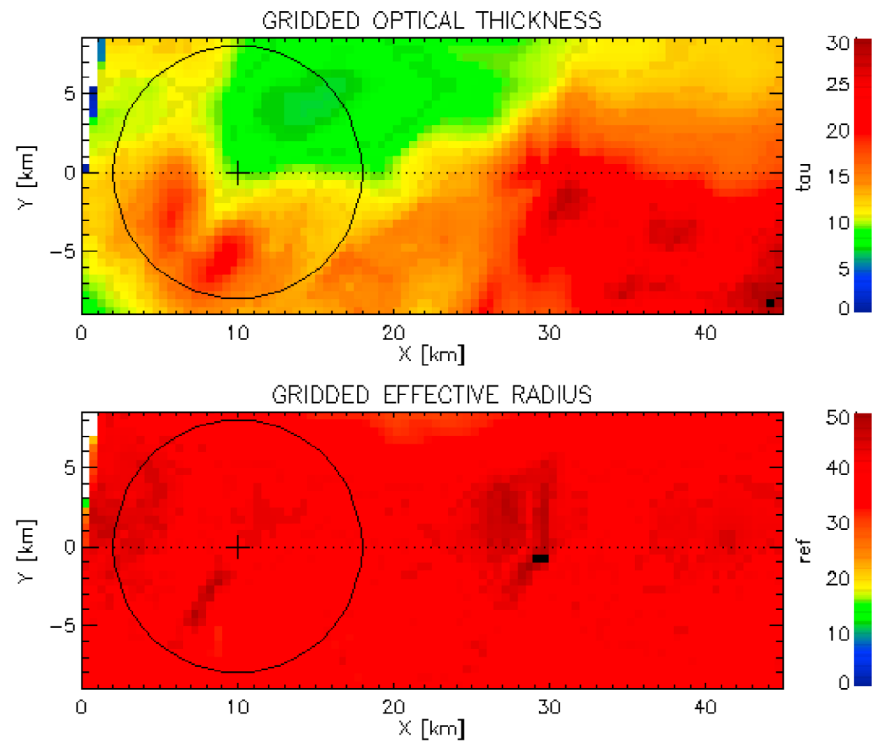


Figure 8. The MAS retrieval of optical thickness and effective radius are shown ($\mu = 0.88$) with the SSFR half-power point (circle) over-plotted.

20 km. Figure 8 shows the retrieved MAS optical thickness and effective radius from $\mu = 0.88$. The circle overlying the left part of the image represents the half-power region of an SSFR measurement. For the time series of retrieved optical properties (Figure 8), the circle was stepped down the image by one scan line, and a new average calculated. This time (flight) series of averages are compared for the two different instruments. Unlike the SSFR, which uses measured downward irradiance to calculate the albedo, the MAS-derived reflectance relies on absolute radiometric calibration and a top-of-atmosphere solar irradiance spectrum.

[32] In Figure 9 the time series of retrieved optical thickness and effective radius are shown for the four cases. For all cases, MAS optical thickness retrievals are greater than those from SSFR; conversely, effective radius retrieved by SSFR is nearly always greater. Because SSFR views an entire hemisphere, in nearly all cases this includes some unknown fraction of open water. GOES visible imagery near coincident with the flight of the ER-2 confirms that this was the case for the three moderate optical thickness cases. This may explain the consistent bias of higher optical thickness retrieved by MAS relative to SSFR. In general these differences are small; the average difference is 2–3 in optical thickness and 2–3 μm in effective radius. For short periods of time the differences can reach up to 12. The largest absolute difference occurs in the high optical thickness case $\mu = 0.92$. The GOES image for the high optical thickness case had a much more extensive and uniform cloud field and spatial sampling differences is a less likely explanation for the differences between MAS and SSFR. As the optical thickness increases, the albedo approaches its asymptotic limit. This means that small changes in albedo or reflectance (or radiometric calibration)

produce large changes in retrieved optical thickness. This is consistent with the finding here that the largest differences in optical thickness were found at relatively high values of optical thickness. For the high optical thickness case, a 10% change in the SSFR irradiance (10% reduction in downwelling irradiance or a 10% increase in the upwelling irradiance or some combination thereof) is needed to bring it into general agreement with the MAS measurements of optical thickness. A summary of the average differences between the irradiance- and radiance-based retrievals and their standard deviations is given in Table 1. The 5% SSFR uncertainty has been propagated in the retrieval to estimate the uncertainty range of the optical thickness and effective radius derived from the SSFR measurements. The MAS uncertainties, expressed as percentages, were averaged in the same way that the values of optical thickness and effective radius were and a grand average of the flight track for each case is quoted. For the moderate optical thickness cases the MAS uncertainties in optical thickness are approximately 20%. For the high optical case the uncertainty reaches 99%. This is a result of the large retrieval sensitivity in that part of the optical thickness space [e.g., Pincus *et al.*, 1995] and should not be taken as quantitatively meaningful. The uncertainties for MAS effective radius are 7–10% in all cases. The uncertainties for both MAS and SSFR are included in Table 1.

[33] The variability of optical thickness and effective radius over a flight segment is higher for MAS, indicating that even after averaging the MAS values, the radiative smoothing from SSFR is greater still. This is not unexpected, as a large fraction of the energy incident on the SSFR originates from outside the swath of MAS. In addition, because the effects of scattering are more pronounced at the shortest wavelengths

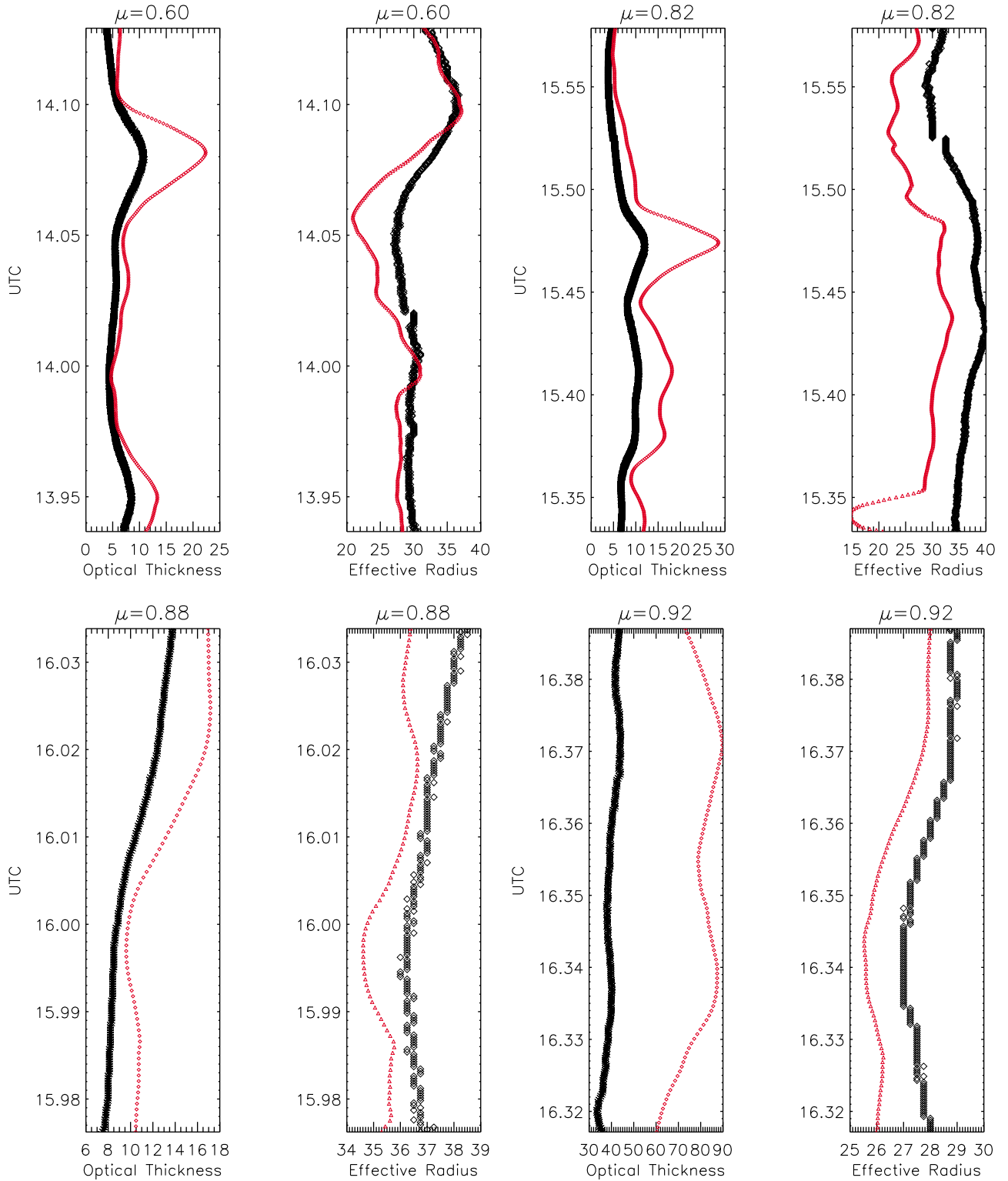


Figure 9. The time series of optical thickness and effective radius retrieved by SSFR (black) and MAS (red) are shown for the four cases.

(conservative scattering), the variation in retrieved optical thickness is greater owing to a greater contribution to the signal from outside the view of MAS. Figure 10 shows the differences between measured spectral albedo from SSFR from modeled spectral albedo derived using the MAS-

retrieved optical thickness and effective radius. The differences are greater than those derived from the two-wavelength SSFR retrievals (Figure 5). The bias in optical thickness retrieval produces a MAS-derived spectral albedo that is generally higher in the visible. For the moderately absorbing

Table 1. Summary of Optical Thickness and Effective Radius for the Four Cases^a

(μ)	MAS Optical Thickness	MAS Effective Radius	SSFR Optical Thickness	SSFR Effective Radius	Optical Thickness Difference (SSFR-MAS)	Effective Radius Difference (μm)	SSFR Optical Thickness +/- 5% Mean Uncertainty	SSFR Effective Radius +/- 5% Mean Uncertainty	MAS Optical Thickness Mean Uncertainty (%)	MAS Effective Radius Mean Uncertainty (%)
0.60	8.29 (4.39)	27.95 (4.05)	5.63 (2.02)	30.43 (2.53)	-2.67 (2.55)	2.48 (2.50)	5.17–6.15	29.26–31.31	20.0	7.9
0.82	12.49 (5.53)	27.53 (4.55)	7.64 (2.47)	30.57 (3.06)	-4.85 (3.32)	3.04 (3.11)	8.82–10.47	29.45–31.80	20.2	10.6
0.88	12.92 (2.96)	35.74 (0.63)	10.19 (2.07)	36.93 (0.63)	2.73 (1.07)	1.19 (0.43)	9.58–11.11	35.66–38.17	18.5	7.2
0.92	80.42 (7.47)	26.63 (0.89)	39.92 (2.65)	27.91 (0.70)	-40.48 (1.30)	1.28 (0.07)	32.44–53.24	26.77–29.03	99.4	8.4

^aValues in parentheses are the mean (standard deviation).

spectral region from 1500 to 2100 nm the differences are reduced and are generally within 0.05; for $\mu = 0.88$ case the differences are even lower, between 0.01 and 0.02. Condensed water is weakly absorbing at these wavelengths so scattering is reduced, resulting in smaller contributions from outside of the MAS swath and better agreement. This is likely scene dependent, with the presence or absence of

clouds outside the MAS field of view also determining in part the level of agreement.

[34] In Figure 11, the SSFR and MAS retrievals of optical thickness and effective radius are compared for each case. The order is sequential in cosine of solar zenith angle: top, $\mu = 0.60$; bottom, $\mu = 0.92$. Figure 11 shows comparisons of retrieved optical thicknesses, the retrieved effective radii, and

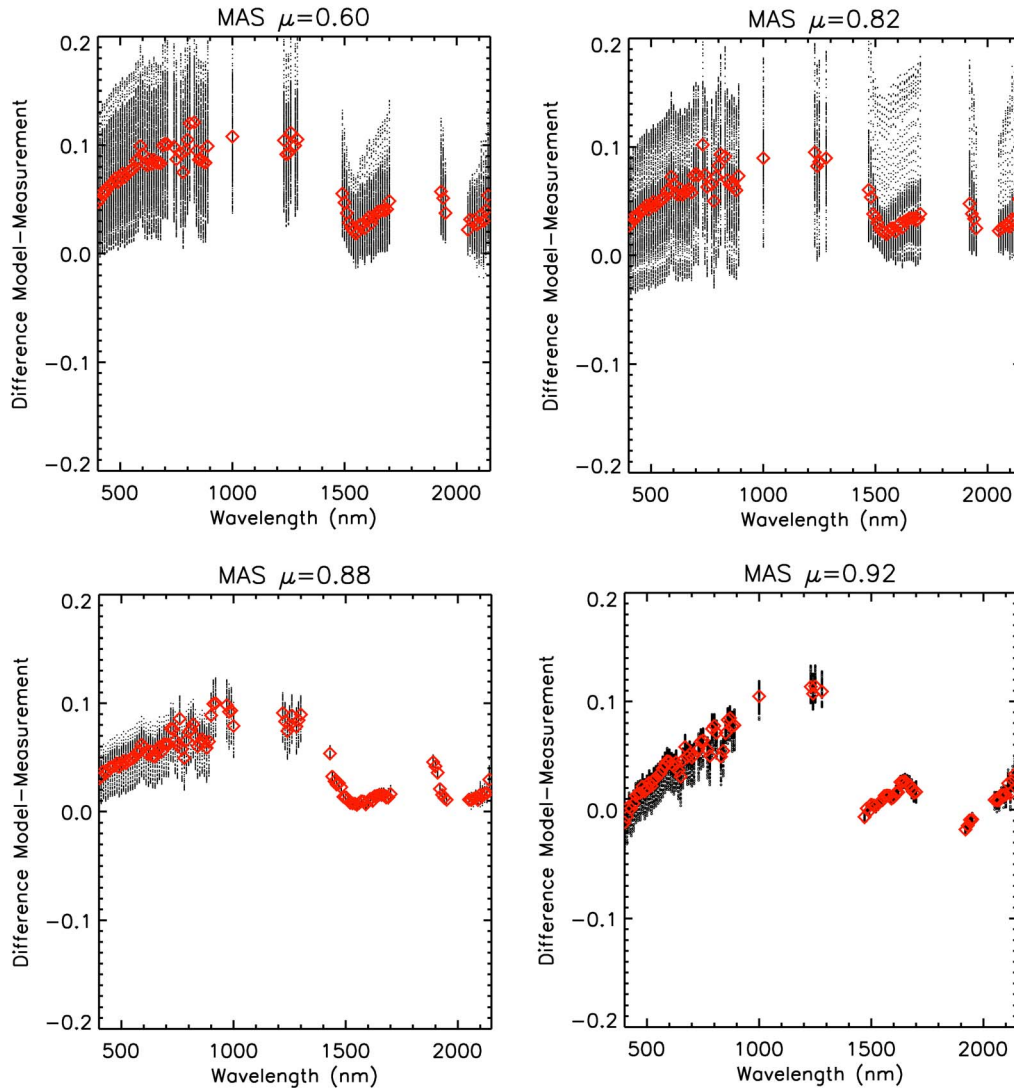


Figure 10. For each of the four cases the differences between modeled (C5) and measured albedo using MAS-derived optical thickness and effective radius are shown. The black dots are the differences for every line in the MAS flight track, and the red diamonds are the mean differences.

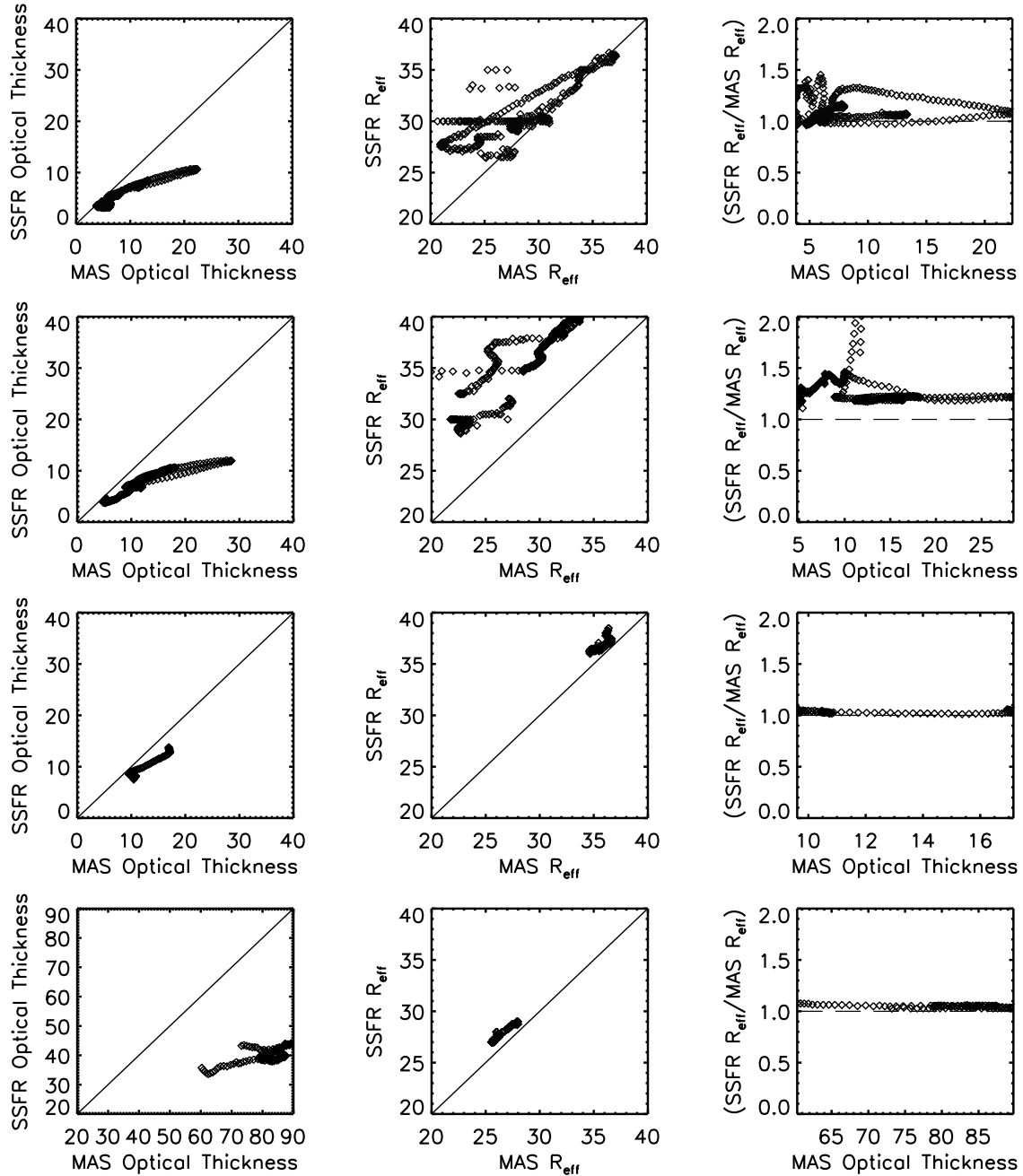


Figure 11. Optical thickness and effective radius as retrieved by SSFR and MAS are plotted against each other as is the ratio of effective radii from SSFR and MAS against optical thickness. The first row is $\mu = 0.60$, the second row $\mu = 0.82$, the third row $\mu = 0.88$, and the fourth row $\mu = 0.92$.

the ratios of the effective radii retrieved by SSFR to that retrieved by MAS plotted against the retrieved optical thickness from MAS. The plots of retrieved optical thicknesses show a bias of higher optical thickness retrieved from MAS; this bias increases as the optical thickness increases. This is most evident in the last row ($\mu = 0.92$) where the optical thicknesses are 3–4 times greater than those in the other three cases and deviation from the one to one line is substantial. The effective radius plots also indicate a bias, as was stated previously, of larger effective radii retrieved by SSFR. In the effective radii ratios versus optical thickness for optical thicknesses less than 20 the differences in effective

radii are large, up to 50%, (excluding the brief departure of 200% in the $\mu = 0.82$ case which may be the result of underlying liquid water clouds). As the optical thickness increases the agreement in effective radius becomes better. This is true in every case, even the high optical thickness case ($\mu = 0.92$) which agrees to within 10% at an optical thickness of 60 and is within 5% at an optical thickness of 90. For all cases, the agreement is 10% or better when the optical thickness is 22 or greater. For low optical thickness, the influence of surface albedo (dark ocean) is greater, biasing the results to a larger effective radius. The MAS retrieval of cloud optical properties, because it is spatially resolved, rejected

pixels that are cloud free. As optical thickness increases, in relatively planar ice clouds, the effects of cloud heterogeneity and surface albedo are less important and the agreement becomes better. Despite the differences in the spatial averaging, and potential differences in radiometric calibration, the MAS retrievals reproduce the observed spectral albedo to within 0.10 across the entire spectrum. In the most spatially uniform case ($\mu = 0.88$) the differences are considerably smaller. A radiometric offset between SSFR and MAS would also contribute to the differences in the retrievals between the two instruments. Similar comparisons to those presented in this study could be made with MODIS coverage to provide a better spatial context with which to judge the total contribution of cloud to the SSFR signal but would be hampered by differences in temporal sampling. The coincidence of satellite, aircraft, and cloud conditions did not allow for such a comparison in this study.

6. Summary

[35] Optical remote sensing of the microphysical and optical properties of ice clouds from satellites has focused on the retrieval of the two cloud properties necessary, but not always sufficient, to completely specify the inputs into radiative transfer models to recreate the spectral albedo: cloud optical thickness and effective cloud particle radius. These retrievals ultimately rely on models of bulk ice cloud single-scattering properties of ice particles to determine the values of optical thickness and effective radius. If the single-scattering parameters are correct or at least spectrally consistent and the retrieval is robust, then the retrieval results can be used in radiative transfer models to correctly model the complete spectral albedo.

[36] In the first part of this work, a test of the ice crystal single-scattering properties used in MODIS Collection 4 and Collection 5 ice-scattering libraries was performed. The optical thickness and effective radius were retrieved using a two-wavelength fit similar to that used by satellites (MODIS) or its airborne proxy (MAS). The retrieved values were derived from the SSFR measurements to remove biases owing to spatial sampling differences between SSFR and MAS. In addition, SSFR measured upwelling and downwelling irradiance, reducing the errors that might occur from absolute radiometric calibration errors. This was a more rigorous test of the model ice single-scattering properties. The retrieved effective radius and optical thickness were subsequently used to predict the measured spectral albedo. The measured and modeled spectral albedo were found to be in very good agreement, especially for the longer wavelengths (1500–2100 nm) where the albedo differences were within 0.02–0.03 over the four flight segments, with a range in effective radius from 25 to 40 μm . The optical thicknesses showed larger differences, yet produced differences between modeled and measured albedo spectra that were within 0.05.

[37] In general the disagreement was largest at shorter wavelengths, up to 0.09 for the high optical thickness case ($\mu = 0.92$). Examination of lidar data for this case did not contain evidence of aerosol above the cloud layer. The spectra for the three lower optical depth cases show good agreement in the shortest wavelengths indicating that the molecular scattering was likely correctly calculated in the radiative transfer model. Ice-scattering properties may be a source of

error although at lower optical thickness the model and measurements agree quite well. Another possible explanation for the discrepancy is the effect a spherical atmosphere which is not accounted for in the calculations performed in this study [Loeb *et al.*, 2002]. This will be investigated with a radiative transfer code that includes the effects of a spherical atmosphere. In any case, it is difficult to draw a firm conclusion on the basis of a single high optical thickness case.

[38] The greatest systematic discrepancy between the measurements and models was for the wavelength region between 1200 nm and 1300 nm. In the lowest optical thickness cases the agreement was consistent with adjacent spectral bands. As the optical thickness increased, the differences were more pronounced. In the highest optical thickness case, the albedo bias approached 0.10. The increasing error with increasing optical thickness may suggest that the model single-scattering albedo is too high in this spectral region. The increase in multiple scattering amplifies absorption and could lead to a discrepancy such as is seen here. The updated refractive indices for ice have not changed in the 1000 to 1300 nm spectral range with the new compilation of Warren and Brandt [2008] although the values have changed in longer wavelengths of 1400 to 2200 nm spectral range. The reason for this discrepancy remains unresolved.

[39] In the second part of this paper we examined the retrievals from MAS, a satellite-like sensor. The MAS retrievals of optical thickness and effective radius were used with the radiative transfer model to predict the spectral albedo. This is a more challenging task for two reasons: unlike the SSFR, the MAS instrument relies on its absolute radiometric calibration to accurately predict reflectance and to determine optical thickness and effective radius. It also measures radiance over a finite swath width, whereas SSFR measures irradiance over a hemisphere. This introduces spatial sampling differences which cannot be completely resolved. Nevertheless, averaging the derived optical properties over the half-power point of SSFR, reproduces the majority of spectral albedo to within 0.05 with the greatest differences occurring in the 400–1200 wavelength range where scattering is greatest and the differences in spatially sampling are exacerbated. For the longer wavelengths, greater than 1500 nm, the agreement is better, in the range of 0.03 or less. A comparison of the retrieved optical thickness and effective radius from SSFR and MAS shows an average absolute deviation of 2.76 in optical thickness and 2.24 μm in effective radius for the three cases of low to moderate optical thickness. The high optical thickness case shows a much greater difference of 40.5 in optical thickness and 1.3 μm in effective radius. At these high optical thicknesses, the retrieval (optical thickness value) is highly sensitive to small changes in radiance (irradiance) as albedo reaches its asymptotic limit. The differences are systematic between MAS and SSFR with MAS nearly always retrieving a higher optical thickness and SSFR nearly always retrieving a larger effective radius. This could be explained by a radiometric calibration error; small differences in the radiometric calibration would produce the largest changes in optical thickness when optical thickness is already high. Additionally, the SSFR hemispherical field of view nearly always includes some fraction of open water. Examination of GOES satellite data confirmed this was the case for the three low to moderate optical thickness cases. This would also lead to SSFR

retrieving a smaller optical thickness and a larger effective radius compared to MAS. The high optical thickness case showed a more extensive cloud field and open water within the view of the SSFR instrument was reduced or absent. Spatial sampling differences prevent any definitive answer to this discrepancy, and in any case, the overall effect was relatively small when calculating spectral albedo.

[40] The role of single-scattering properties of ice crystals are crucial in satellite retrievals of ice cloud properties and ultimately for radiative transfer calculations and their inclusion in ice cloud modeling in climate models. We have examined here the spectral consistency of these properties within the solar spectrum and over a range of solar zenith angles and optical thicknesses encountered during TC⁴. We have validated the fidelity of the derived properties of optical thickness and effective radius on the basis of ice single-scattering properties to recreate the spectral albedo when used in a radiative transfer model. Spectral irradiance is the fundamental unit of energy balance; by comparing multi-spectral retrievals of cloud optical thickness and effective radius, with hyperspectral irradiance we can be confident that the ice single-scattering properties are robust. These calculations are of importance for cloud radiative budget studies and ultimately climate models. It is through tests such as the one performed here that we can be confident that satellite retrievals of optical thickness and effective radius can be accurately extrapolated to spectral albedo for the entire solar spectrum. New models from the same authors of the single-scattering properties used here have been developed for ice crystals with varying surface morphologies, from smooth to rough and substantially roughened ice crystals. These models will have continuous spectral sampling over the range of the SSFR instrument. They also include updated values for the ice optical constants. These new libraries will be compared with the same cases shown here to determine their ability to accurately reproduce spectral albedo and to examine the impact on the retrieval of ice cloud optical properties.

[41] **Acknowledgments.** Bruce Kindel was supported through a NASA grant (NNX07AL12G). Bryan Baum acknowledges support through a NASA grant (NNX08AF81G). MAS analysis was made possible with support from various elements of the NASA Radiation Sciences Program. The authors wish to thank Warren Gore and Tony Trias (NASA Ames Research Center) for their support of SSFR during TC⁴, and Tom Arnold and Galina Wind (NASA Goddard Research Center) for their help with MAS data analysis.

References

- Baran, A. J. (2004), On the scattering and absorption properties of cirrus cloud, *J. Quant. Spectrosc. Radiat. Transfer*, **89**, 17–36, doi:10.1016/j.jqsrt.2004.05.008.
- Baran, A. J. (2009), A review of the light scattering properties of cirrus, *J. Quant. Spectrosc. Radiat. Transfer*, **110**, 1239–1260.
- Baran, A. J., and P. N. Francis (2004), On the radiative properties of cirrus cloud at solar and thermal wavelengths: A test of model consistency using high-resolution airborne radiance measurements, *Q. J. R. Meteorol. Soc.*, **130**, 763–778, doi:10.1256/qj.03.151.
- Baran, A. J., and S. Havemann (2004), The dependence of retrieved cirrus ice-crystal effective dimension on assumed ice-crystal geometry and size-distribution function at solar wavelengths, *Q. J. R. Meteorol. Soc.*, **130**, 2153–2167, doi:10.1256/qj.03.154.
- Baran, A. J., and L.-C. Labonnote (2007), A self consistent scattering model for cirrus. I: The solar region, *Q. J. R. Meteorol. Soc.*, **133**, 1899–1912, doi:10.1002/qj.164.
- Baran, A. J., P. Watts, and P. Francis (1999), Testing the coherence of cirrus microphysical and bulk properties retrieved from dual-viewing multispectral satellite radiance measurements, *J. Geophys. Res.*, **104**, 31,673–31,683, doi:10.1029/1999JD900842.
- Baran, A. J., P. N. Francis, L.-C. Labonnote, and M. Doutriaux-Boucher (2001), A scattering phase function for ice cloud: Tests of applicability using aircraft and satellite multi-angle multi-wavelength radiance measurements of cirrus, *Q. J. R. Meteorol. Soc.*, **127**, 2395–2416, doi:10.1002/qj.49712757711.
- Baran, A. J., S. Havemann, P. N. Francis, and P. D. Watts (2003), A consistent set of single-scattering properties for cirrus cloud: Tests using radiance measurements from a dual-viewing multi-wavelength satellite-based instrument, *J. Quant. Spectrosc. Radiat. Transfer*, **79–80**, 549–567, doi:10.1016/S0022-4073(02)00307-2.
- Baum, B. A., D. P. Kratz, P. Yang, S. C. Ou, Y. Hu, P. F. Soulen, and S.-C. Tsay (2000), Remote sensing of cloud properties using MODIS airborne simulator imagery during SUCCESS 1. Data and models, *J. Geophys. Res.*, **105**, 11,767–11,780, doi:10.1029/1999JD901089.
- Baum, B. A., P. Yang, A. J. Heymsfield, S. Platnick, M. D. King, Y.-X. Hu, and S. T. Bedka (2005), Bulk scattering properties for the remote sensing of ice clouds. part II: Narrowband models, *J. Appl. Meteorol.*, **44**, 1896–1911, doi:10.1175/JAM2309.1.
- Bergstrom, R. W., P. Pilewskie, B. Schmid, and P. B. Russell (2003), Estimates of the spectral aerosol single scattering albedo and aerosol radiative effects during SAFARI 2000, *J. Geophys. Res.*, **108**(D13), 8474, doi:10.1029/2002JD002435.
- Bodhaine, B. A., N. B. Wood, E. G. Dutton, and J. R. Slusser (1999), On Rayleigh optical depth calculations, *J. Atmos. Oceanic Technol.*, **16**, 1854–1861, doi:10.1175/1520-0426(1999)016<1854:ORODC>2.0.CO;2.
- Bohren, C. F., and D. R. Huffman (1983), *Absorption and Scattering of Light by Small Particles*, John Wiley, New York.
- Chen, T., W. B. Rossow, and Y. C. Zhang (2000), Radiative effects of cloud-type variations, *J. Clim.*, **13**, 264–286, doi:10.1175/1520-0442(2000)013<0264:REOCTV.2.0.CO;2.
- Coddington, O., K. S. Schmidt, P. Pilewskie, W. J. Gore, R. W. Bergstrom, M. Roman, J. Redemann, P. B. Russell, J. Liu, and C. C. Schaaf (2008), Aircraft measurements of spectral surface albedo and its consistency with ground-based and space-borne observations, *J. Geophys. Res.*, **113**, D17209, doi:10.1029/2008JD010089.
- Cooper, S. J., T. S. L'Ecuyer, P. Gabriel, A. J. Baran, and G. L. Stephens (2006), Objective assessment of the information content of visible and infrared radiance measurements for cloud microphysical property retrievals over the global oceans. part II: Ice clouds, *J. Appl. Meteorol. Climatol.*, **45**, 42–62, doi:10.1175/JAM2327.1.
- Ebert, E. E., and J. A. Curry (1992), A parameterization of ice cloud optical properties for climate models, *J. Geophys. Res.*, **97**, 3831–3836.
- Edwards, J. M., S. Havemann, J. C. Thelen, and A. J. Baran (2007), Parameterization for the radiative properties of ice crystals: Comparison with existing schemes and impact in a GCM, *Atmos. Res.*, **83**, 19–35, doi:10.1016/j.atmosres.2006.03.002.
- Ehrlich, A., M. Wendisch, E. Bierwirth, J. -F. Gayer, G. Minoche, A. Lampert, and B. Mayer (2009), Evidence of ice crystals at cloud top of Arctic boundary-layer mixed-phase clouds derived from airborne remote sensing, *Atmos. Chem. Phys.*, **9**, 9401–9416, doi:10.5194/acp-9-9401-2009.
- Fu, Q. (2007), A new parameterization of an asymmetry factor of cirrus clouds for climate models, *J. Atmos. Sci.*, **64**, 4140–4150, doi:10.1175/2007JAS2289.1.
- Havemann, S., and A. J. Baran (2004), Calculation of the phase matrix elements of elongated hexagonal ice columns using the T-matrix method, *J. Quant. Spectrosc. Radiat. Transfer*, **89**, 87–96, doi:10.1016/j.jqsrt.2004.05.014.
- Hook, S. J., K. J. Thome, M. Fitzgerald, and A. B. Kahle (2001), The MODIS/ASTER airborne simulator (MASTER)—A new instrument for earth science studies, *Remote Sens. Environ.*, **76**, 93–102, doi:10.1016/S0034-4257(00)00195-4.
- Hu, X.-Y., B. Wielicki, B. Lin, G. Gibson, S.-C. Tsay, K. Stamnes, and T. Wong (2000), δ -Fit: A fast and accurate treatment of particle scattering phase functions with weighted singular-value decomposition least-squares fitting, *J. Quant. Spectrosc. Radiat. Transfer*, **65**, 681–690, doi:10.1016/S0022-4073(99)00147-8.
- Jensen, E. J., and O. B. Toon (1994), Tropical cirrus cloud radiative forcing: Sensitivity studies, *Geophys. Res. Lett.*, **21**, 2023–2026, doi:10.1029/94GL01358.
- Jensen, E. J., D. Starr, and O. B. Toon (2004), Mission investigates tropical cirrus clouds, *Eos Trans. AGU*, **85**, 45–49.
- Jensen, E. J., et al. (2009), On the importance of small ice crystals in tropical anvil cirrus, *Atmos. Chem. Phys. Disc.*, **9**, 5321–5370, doi:10.5194/acpd-9-5321-2009.
- Jiang, J. H., H. Su, S. T. Massie, P. R. Colarco, M. R. Schoeberl, and S. Platnick (2009), Aerosol-CO relationship and aerosol effect on ice

- cloud particle size: Analyses from Aura Microwave Limb Sounder and Aqua Moderate Resolution Imaging Spectroradiometer observations, *J. Geophys. Res.*, **114**, D20207, doi:10.1029/2009JD012421.
- Jin, Z., T. P. Charlock, W. L. Smith, and K. Rutledge (2004), A parameterization of ocean surface albedo, *Geophys. Res. Lett.*, **31**, L22301, doi:10.1029/2004GL021180.
- Joseph, J. H., W. J. Wiscombe, and J. A. Weinman (1976), The delta-Eddington approximation for radiative flux transfer, *J. Atmos. Sci.*, **33**, 2452–2459, doi:10.1175/1520-0469(1976)033<2452:TDEAFR>2.0.CO;2.
- King, M. D., Y. J. Kaufman, W. P. Menzel, and D. Tanre (1992), Remote sensing of cloud, aerosol, and water vapor properties from the moderate resolution imaging spectrometer (MODIS), *IEEE Trans. Geosci. Remote Sens.*, **30**, 2–27, doi:10.1109/36.124212.
- King, M. D., S. C. Tsay, S. E. Platnick, M. Wang, and K. N. Liou (1997), Cloud retrieval algorithms for MODIS: Optical thickness, effective particle radius, and thermodynamic phase, *MODIS Algorithm Theor. Basis Doc. ATBD-MOD-05*, 79 pp., NASA Goddard Space Flight Cent., Greenbelt, Md. (Available at modis-atmos.gsfc.nasa.gov/docs/atbd_mod05.pdf).
- King, M. D., S. Platnick, P. Yang, G. T. Arnold, M. A. Gray, J. C. Riedi, S. A. Ackerman, and K. N. Liou (2004), Remote sensing of liquid water and ice cloud optical thickness and effective radius in the Arctic: Application of airborne multispectral MAS data, *J. Atmos. Oceanic Technol.*, **21**, 857–875, doi:10.1175/1520-0426(2004)021<0857:RSOLWA>2.0.CO;2.
- King, M. D., S. Platnick, G. Wind, G. T. Arnold, and R. T. Dominguez (2010), Remote sensing of the radiative and microphysical properties of clouds during TC⁴: Results from MAS, MASTER, MODIS, and MISR, *J. Geophys. Res.*, **115**, D00J07, doi:10.1029/2009JD013277.
- Kurucz, R. L. (1992), Synthetic infrared spectra, in *Infrared Solar Physics: Proceedings of the 154th Symposium of the International Astronomical Union*, edited by D. M. Rabin, J. T. Jefferies, and C. Lindsey, pp. 523–531, Kluwer Acad., Dordrecht, the Netherlands.
- Lacis, A. A., and V. Oinas (1991), A description of the correlated-k distribution method for modeling nongray gaseous absorption, thermal emission, and multiple scattering in vertically inhomogeneous atmospheres, *J. Geophys. Res.*, **96**, 9027–9063, doi:10.1029/90JD01945.
- Loeb, N. G., S. Kato, and B. A. Wielicki (2002), Defining top-of-the-atmosphere flux reference level for Earth radiation budget studies, *J. Clim.*, **15**, 3301–3309, doi:10.1175/1520-0442(2002)015<3301:DTOTAF>2.0.CO;2.
- Macke, A., J. Muller, and E. Raschke (1996), Single scattering properties of atmospheric crystals, *J. Atmos. Sci.*, **53**, 2813–2825, doi:10.1175/1520-0469(1996)053<2813:SSPOAI>2.0.CO;2.
- McFarquhar, G. M., and A. J. Heymsfield (1998), The definition and significance of an effective radius for ice clouds, *J. Atmos. Sci.*, **55**, 2039–2052, doi:10.1175/1520-0469(1998)055<2039:TDASOA>2.0.CO;2.
- McFarquhar, G. M., J. Um, M. Freer, D. Baumgardner, G. L. Kok, and G. Mace (2007), Importance of small ice crystals to cirrus properties: Observations from the Tropical Warm Pool International Cloud Experiment (TWP-ICE), *Geophys. Res. Lett.*, **34**, L13803, doi:10.1029/2007GL029865.
- Mishchenko, M., W. Rossow, A. Macke, and A. Lacis (1996), Sensitivity of cirrus cloud albedo, bidirectional reflectance, and optical thickness retrieval accuracy to ice particle shape, *J. Geophys. Res.*, **101**, 16,973–16,985, doi:10.1029/96JD01155.
- Mitchell, D. L. (2002), Effective diameter in radiation transfer: General definition, applications, and limitations, *J. Atmos. Sci.*, **59**, 2330–2346, doi:10.1175/1520-0469(2002)059<2330:EDIRTG>2.0.CO;2.
- Nakajima, T., and M. D. King (1990), Determination of the optical thickness and effective particle radius of clouds from reflected solar radiation measurements. part I: Theory, *J. Atmos. Sci.*, **47**, 1878–1893, doi:10.1175/1520-0469(1990)047<1878:DOTOTA>2.0.CO;2.
- Pilewskie, P., J. Pommier, R. Bergstrom, W. Gore, S. Howard, M. Rabbette, B. Schmid, P. V. Hobbs, and S. C. Tsay (2003), Solar spectral radiative forcing during the Southern African Regional Science Initiative, *J. Geophys. Res.*, **108**(D13), 4846, doi:10.1029/2002JD002411.
- Pincus, R., M. Szczodrak, J. Gu, and P. Austin (1995), Uncertainty in cloud optical depth made from satellite radiance measurements, *J. Clim.*, **8**, 1453–1462, doi:10.1175/1520-0442(1995)008<1453:UICODE>2.0.CO;2.
- Platnick, S. (2000), Vertical photon transport in cloud remote sensing problems, *J. Geophys. Res.*, **105**, 22,919–22,935, doi:10.1029/2000JD900333.
- Platnick, S. (2001), Approximations for horizontal photon transport in cloud remote sensing problems, *J. Quant. Spectrosc. Radiat. Transfer*, **68**, 75–99, doi:10.1016/S0022-4073(00)00016-9.
- Platnick, S., M. D. King, S. A. Ackerman, W. P. Menzel, B. A. Baum, J. C. Riedi, and R. A. Frey (2003), The MODIS cloud products: Algorithms and examples from Terra, *IEEE Trans. Geosci. Remote Sens.*, **41**, 459–473, doi:10.1109/TGRS.2002.808301.
- Ramanathan, V., R. D. Cess, E. F. Harrison, P. Minnis, B. R. Barkstrom, E. Ahmad, and D. Hartmann (1989), Cloud-radiative forcing and climate—Results from the Earth Radiation Budget Experiment, *Science*, **243**, 57–63, doi:10.1126/science.243.4887.57.
- Rothman, L., et al. (2005), The HITRAN 2004 molecular spectroscopic database, *J. Quant. Spectrosc. Radiat. Transfer*, **96**, 139–204, doi:10.1016/j.jqsrt.2004.10.008.
- Schmidt, K. S., P. Pilewskie, S. Platnick, G. Wind, P. Yang, and M. Wendisch (2007), Comparing irradiance fields derived from Moderate Resolution Imaging Spectroradiometer airborne simulator cirrus cloud retrievals with solar spectral flux radiometer measurements, *J. Geophys. Res.*, **112**, D24206, doi:10.1029/2007JD008711.
- Stamnes, K., S.-C. Tsay, W. Wiscombe, and K. Jayaweera (1988), Numerically stable algorithm for discrete-ordinate-method radiative transfer in multiple scattering and emitting layered media, *Appl. Opt.*, **27**, 2502–2509, doi:10.1364/AO.27.002502.
- Stephens, G. L., S.-C. Tsay, P. W. Stackhouse Jr., and P. J. Flatau (1990), The relevance of the microphysical and radiative properties of cirrus clouds to climate and climatic feedback, *J. Atmos. Sci.*, **47**, 1742–1754, doi:10.1175/1520-0469(1990)047<1742:TROTMA>2.0.CO;2.
- Takano, Y., and K. N. Liou (1989), Solar radiative transfer in cirrus clouds. part I: Single-scattering and optical properties of hexagonal ice crystals, *J. Atmos. Sci.*, **46**, 3–19, doi:10.1175/1520-0469(1989)046<0003:SRITIC>2.0.CO;2.
- Toon, O. B., et al. (2010), Planning, implementation, and first results of the Tropical Composition, Cloud and Climate Coupling Experiment (TC⁴), *J. Geophys. Res.*, **115**, D00J04, doi:10.1029/2009JD013073.
- Twomey, S., and T. Cocks (1982), Spectral reflectance of clouds in the near-infrared: Comparison of measurements and calculations, *J. Meteorol. Soc. Jpn.*, **60**, 583–592.
- Ulanowski, Z., E. Hesse, P. H. Kaye, and A. J. Baran (2006), Light scattering by complex ice-analogue crystals, *J. Quant. Spectrosc. Radiat. Transfer*, **100**, 382–392, doi:10.1016/j.jqsrt.2005.11.052.
- Waliser, D. E., et al. (2009), Cloud ice: A climate model challenge with signs and expectations of progress, *J. Geophys. Res.*, **114**, D00A21, doi:10.1029/2008JD010015.
- Warren, S. G. (1984), Optical constants of ice from the ultraviolet to the microwave, *Appl. Opt.*, **23**, 1206–1225, doi:10.1364/AO.23.001206.
- Warren, S. G., and R. E. Brandt (2008), Optical constants of ice from the ultraviolet to the microwave: A revised compilation, *J. Geophys. Res.*, **113**, D14220, doi:10.1029/2007JD009744.
- Wendisch, M., P. Pilewskie, J. Pommier, S. Howard, P. Yang, A. J. Heymsfield, C. G. Schmitt, D. Baumgardner, and B. Mayer (2005), Impact of cirrus crystal shape on solar spectral irradiance: A case study for subtropical cirrus, *J. Geophys. Res.*, **110**, D03202, doi:10.1029/2004JD005294.
- Wiscombe, W. (1977), The delta-M method: Rapid yet accurate radiative flux calculation for strongly asymmetric phase functions, *J. Atmos. Sci.*, **34**, 1408–1422, doi:10.1175/1520-0469(1977)034<1408:TDMRYA>2.0.CO;2.
- Yang, P., and K. N. Liou (1996), Geometric-Optics-integral-equation method for light scattering by nonspherical ice crystals, *Appl. Opt.*, **35**, 6568–6584.
- Yang, P., and K. N. Liou (1998), Single-scattering properties of complex ice crystals in terrestrial atmosphere, *Contrib. Atmos. Phys.*, **71**, 223–248.
- Yang, P., K. Liou, and W. Arnott (1997), Extinction efficiency and single-scattering albedo for laboratory and natural cirrus clouds, *J. Geophys. Res.*, **102**, 21,825–21,835, doi:10.1029/97JD01768.
- Yang, P., B. A. Baum, A. J. Heymsfield, Y. X. Hu, H.-L. Huang, S.-C. Tsay, and S. Ackerman (2003), Single-scattering properties of droxtals, *J. Quant. Spectrosc. Radiat. Transfer*, **79–80**, 1159–1169, doi:10.1016/S0022-4073(02)00347-3.
- Yang, P., L. Zhang, S. L. Nasiri, B. A. Baum, H.-L. Huang, M. D. King, and S. Platnick (2007), Differences between collection 4 and 5 MODIS ice cloud optical/microphysical products and their impact on radiative forcing simulations, *IEEE Trans. Geosci. Remote Sens.*, **45**, 2886–2899, doi:10.1109/TGRS.2007.898276.

B. A. Baum, Space Science and Engineering Center, University of Wisconsin-Madison, Madison, WI 53706, USA.

B. C. Kindel and P. Pilewskie, Laboratory for Atmospheric and Space Physics, Department of Atmospheric and Oceanic Sciences, University of Colorado at Boulder, C.B. 392, Boulder, CO 80309-0392, USA. (kindel@lasp.colorado.edu)

S. Platnick, NASA Goddard Space Flight Center, Greenbelt, MD 20771, USA.

K. S. Schmidt, Department of Atmospheric and Oceanic Sciences, University of Colorado at Boulder, Boulder, CO 80309, USA.

P. Yang, Department of Atmospheric Sciences, Texas A&M University, College Station, TX 77843, USA.